Nanoscale

Accepted Manuscript

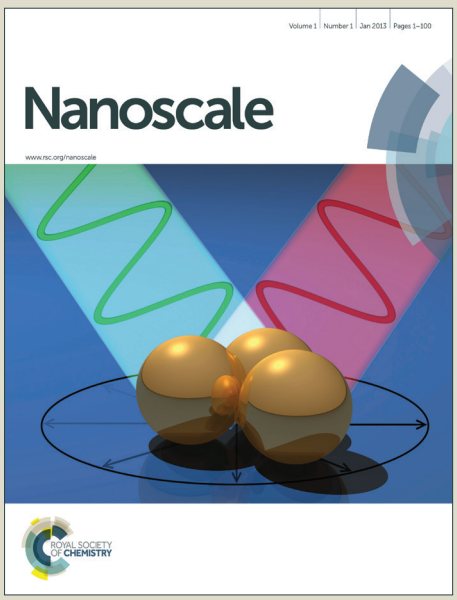

ROYAL SOCIETY OF CHEMISTRY

www.rsc.org/nanoscale

Cite this: DOI: 10.1039/c0xx00000x

www.rsc.org/xxxxxx

ARTICLE TYPE

Exfoliated-SnS_2 Restacked on Graphene as High-Capacity, High-Rate, and Long-Cycle Life Anode for Sodium Ion Batteries

Yongchang Liu, Hongyan Kang, Lifang Jiao,* Chengcheng Chen, Kangzhe Cao, Yijing Wang and Huatang Yuan

Received (in XXX, XXX) Xth XXXXXXXXX 20XX, Accepted Xth XXXXXXXXX 20XX
DOI: 10.1039/b000000x

Designed as a high-capacity, high-rate, and long-cycle life anode for sodium ion batteries, exfoliated-SnS_2 restacked on graphene is prepared by the hydrolysis of lithiated SnS_2 followed by a facile hydrothermal method. Structural and morphological characterizations demonstrate that ultrasmall SnS_2 nanoplates (with typical size of 20-50 nm) composed of 2-5 layers are homogeneously decorated on the surface of graphene, while the hybrid structure self-assembles into a three-dimensional (3D) network architecture. The obtained SnS_2/graphene nanocomposite delivers a remarkable capacity as high as 650 mA h g^{-1} at the current density of 200 mA g^{-1}. More impressively, the capacity can reach 326 mA h g^{-1} even at 4000 mA g^{-1} and remains stable at ~610 mA h g^{-1} without fading up to 300 cycles when the rate is brought back to 200 mA g^{-1}. The excellent electrochemical performance is attributed to the synergetic effects between the ultrasmall SnS_2 and the highly conductive graphene network. The unique structure can simultaneously facilitate Na^+ ions diffusion, provide more reaction sites, and suppress aggregation and volume fluctuation of the active materials during prolonged cycling.

Introduction

Sodium-ion batteries (SIBs), as a substitute for lithium-ion batteries (LIBs), have attracted extensive investigation owing to the natural abundance of sodium.[1-6] The low cost and huge availability of Na compounds give SIBs a potential advantage in large-scale energy storage applications.[7-11] Although the intercalation mechanism of Na in electrode materials is similar to that of Li, the larger size of Na^+ ion (1.02 Å in radius) as compared to Li^+ ion (0.59 Å in radius) makes it difficult to simply adopt the recent strategies proposed for high-performance LIBs.[12-14] The key challenge facing SIBs is to develop appropriate host materials with the capability for fast and stable sodium-ion insertion/extraction.[15,16] In particular, only few of Na-storage anode materials have demonstrated suitable redox capacity and adequate cyclability.[17-20] Thus far, tin and tin-based compounds have shown good prospects as high-capacity SIB anodes, based on the theoretical stoichiometry of $Na_{3.75}Sn$ (847 mA h g^{-1}).[21-25] For example, Liu and co-workers reported a three-dimensional (3D) array of Sn nanorods with a high initial capacity of 722 mA h g^{-1} and ~60% capacity retention after 150 cycles at 50 mA g^{-1}.[26] Anodes based on SnO_2 (432 mA h g^{-1} after 150 cycles at 20 mA g^{-1})[27] and SnO_2@graphene nanocomposite (638 mA h g^{-1} after 100 cycles at 20 mA g^{-1})[28] were later demonstrated by Wang's group. A Sn-SnS-C nanocomposite was also examined as SIB anode, with capacities of 664 mA h g^{-1} at 20 mA g^{-1} and 350 mA h g^{-1} at 800 mA g^{-1}.[29] These are clearly encouraging developments but a high-capacity tin-based anode with high-rate capability and long-cycle life for SIBs is still urgently needed. As the large volume expansion in tin-sodium alloy formation (520% from Sn to $Na_{3.75}Sn$) would lead to a continuous pulverization and aggregation of electrode materials,[21-23] considerable improvements in the design and optimization of anode composition and structure are required.

These considerations have stimulated our research interest into SnS_2, a kind of layered transition metal dichalcogenides (TMDs). SnS_2 has a sandwich structure that consists of covalently bonded S-Sn-S trilayers separated by a relatively large van der Waals interaction.[30,31] Different from graphite, which fails to intercalate sodium effectively due to the mismatching of interlayer distance (d_{002} = 3.34 Å) with large Na^+ ions.[32] SnS_2 has a larger interlayer spacing (d_{002} = 5.90 Å) and can accommodate Na^+ ions to move reversibly with acceptable mobility.[33,34] Moreover, during the sodiation/desodiation process, the generated amorphous NaS_2 acts as an inert matrix surrounding the active Sn grains, thus suppressing the pulverization and aggregation of Na-Sn alloy. Therefore, SnS_2 is an ideal candidate as the anode material for Na-ion batteries.

It is common that layered transition metal disulfides can be exfoliated to single-layer or few-layer sheets, which show distinctively different physical and chemical properties in comparison to their bulk counterparts.[35,36] Indeed, exfoliated MoS_2 has been verified to display open channels for ion diffusion and provide considerable active sites as anode for LIBs.[37,38] To the best of our knowledge, exfoliated SnS_2 has not been reported in battery applications, it is supposed that the more open-framework structure of few-layers can facilitate the transportation of Na^+ ions and ensure the flooding of electrolyte. In addition, graphene is identified to be a versatile material with good

conductivity and mechanical resilience,[39-42] which has been reported to significantly improve the Na-storage ability of SnS_2.[33,34,43,44] It is thus that the exfoliated SnS_2/graphene composite seems to be a promising design aiming at high-capacity, high-rate capability, and long-cycle life Na-storage anode.

Motivated by the above considerations, in this paper, we prepared exfoliated-SnS_2 by the hydrolysis of lithiated SnS_2 ($LiSnS_2$), and then restacked it on graphene *via* a cetyltrimethyl ammonium bromide (CTAB)-assisted hydrothermal method. The preparation procedure is illustrated in Scheme 1. Instrumental characterizations demonstrate that ultrasmall SnS_2 nanoplates (with typical size of 20-50 nm) composed of 2-5 layers are homogeneously decorated on the surface of graphene, while the hybrid structure self-assembles into a 3D network architecture. It was found that the obtained SnS_2/graphene nanocomposite exhibited excellent electrochemical properties in sodium ion batteries, delivering a remarkable capacity as high as 650 mA h g^{-1} at the current density of 200 mA g^{-1}. More impressively, the capacity can reach 326 mA h g^{-1} even at 4000 mA g^{-1} and remains stable at ~610 mA h g^{-1} without fading up to 300 cycles when the rate is brought back to 200 mA g^{-1}.

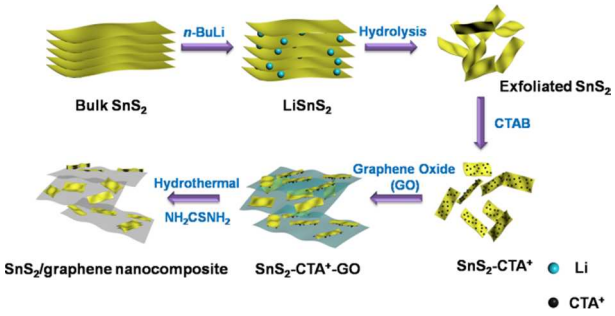

Scheme 1 Schematic illustration of the preparation of SnS_2/graphene nanocomposite.

Experimental Section

Materials Synthesis

In a typical synthesis, commercial bulk SnS_2 (J&K, 99.9%) was soaked in two equivalents butyllithium (Amethyst, *n*-BuLi, 2.4 M in hexane) and kept in argon atmosphere for a week at room temperature. The concentration of *n*-Buli solution was adjusted to 1 M with the addition of anhydrous pentane (Alfa Aesar, 99.8%) before reaction. The product was filtered off in a dry box, washed with pentane and then dried under reduced pressure. The product stoichiometry is known to be $LiSnS_2$. Rapid hydrolysis and sonication of 100 mg $LiSnS_2$ in 15 mL acidulated deionized water (HCl/H_2O = 1/10 in volume) resulted in the formation of exfoliated SnS_2 layers. The released hydrogen flow was speculated to push the adjacent SnS_2 layers further apart. The reactions are described as follows:

$$SnS_2 + n\text{-BuLi} \rightarrow LiSnS_2 + 1/2C_8H_{18}$$
$$LiSnS_2 + H_2O \rightarrow (SnS_2)_{\text{exfoliated layers}} + LiOH + 1/2H_2$$

Then 0.4 mmol cetyltrimethyl ammonium bromide (J&K, CTAB, 99.8%) was fully dissolved in 10 mL deionized (DI) water and added to the exfoliated SnS_2. The mixture was sonicated for 3 h at 40 °C to allow CTA^+ adsorption onto the SnS_2 surface by electrostatic interaction. The SnS_2-CTA^+ layers were highly dispersed in water.

Graphene oxide (GO) was prepared from natural graphite powder (Alfa Aesar, 99 %) by the modified Hummers method.[45] 20 mg as-synthesized GO was well-dispersed in 20 mL DI water with the help of ultrasonication. Then, the GO dispersion was slowly added to the exfoliated SnS_2-CTA^+ suspension, and the mixture was kept under sonication for 2 h to form a brown flocculent precipitate containing SnS_2-CTA^+-GO (the oxygen-containing functional groups on graphene surface would adsorb the SnS_2-CTA^+ layers through electrostatic attraction). This was followed by the addition of 3 mmol thiourea (Acros, NH_2CSNH_2, 99%) as a reducing agent with continued stirring. The reaction mixture was transferred to a 50 mL Teflon-lined autoclave, sealed tightly, and maintained at 150 °C for 48 h. During the hydrothermal process, H_2S, which was released from NH_2CSNH_2 at high temperature, reduced GO to graphene. Simultaneously, the exfoliated SnS_2, which was very sensitive to temperature, would restack turbostratically on the surface of graphene when heating.[37,38] The outer electron orbit of Sn element could also bond with the π electron cloud and residual oxygen-containing functional groups of graphene.[33,38,46] After natural cooling to room temperature, the resulting black-brown precipitate was washed several times with hot DI water (50 °C) to remove CTAB and residual impurities. It was then allowed to dry under suction and freeze-dried, the obtained SnS_2/graphene composite was denoted as SnS_2/G-20. With the same method as above, SnS_2/graphene composites produced by adding 10 and 30 mg GO were also prepared and designated as SnS_2/G-10 and SnS_2/G-30, respectively. As a control, the restacked SnS_2 without any GO or CTAB was also fabricated *via* a hydrothermal procedure. The fabrication process for SnS_2/graphene composite is illustrated with digital photographs in Scheme S1†.

Materials Characterizations

X-ray diffraction (XRD) analysis was performed on a Rigaku D/Max-2500 with Cu-Kα radiation (λ= 1.54178 Å). The 2θ angular region between 3° and 80° was investigated at a scan rate of 2° min^{-1}. The morphology and microstructure were observed by scanning electron microscopy (SEM, HITACHI S-4800) and transmission electron microscopy (TEM, Tecnai G2 F20). The element content of the samples (dried) was analyzed by energy dispersive X-ray spectroscopy (EDS, GENENIS-4000). Fourier transform infrared (FT-IR) spectra of the samples were collected at room temperature on a FTIR-650 spectrometer (Tianjin Gangdong) at a resolution of 4 cm^{-1}. Raman spectroscopy (Renishaw inVia, excitation 514.5 nm) and X-ray photoelectron spectrometer (XPS, PHI 5000 Versaprobe, ULVAC PHI) were also used to characterize the synthesized materials.

Electrochemical Measurements

Electrochemical tests were carried out using CR2032 coin cells assembled in an argon-filled glove box with water and oxygen contents below 5 ppm. The working electrodes were fabricated by mixing 75 wt.% active materials, 15 wt.% super P carbon, and 10 wt.% carboxymethyl cellulose (CMC) binder in distilled water solvent to form homogeneous slurry. The mixture was coated onto copper foil. The coated electrode was dried at 80 °C for 12 h

in a vacuum oven and then pressed. The active material loading was about 1.0-1.5 mg cm^{-2} without deducting the mass of graphene. The counter/reference electrode was sodium metal, and the separator was glass fiber. The electrolyte solution was 1 M $NaClO_4$ dissolved in ethylene carbonate/diethyl carbonate (EC/DEC, 1:1 in volume). Galvanostatic charge/discharge tests were performed between 0.01 and 2.5 V at different rates on a LAND battery-test instrument (CT2001A). The applied current densities were based on the mass of whole SnS_2/graphene composite. Cyclic voltammetry was conducted on a CHI660B electrochemical workstation at a scan rate of 0.1 mV s^{-1} within a potential window of 0.01-2.5 V. Electrochemical impedance spectra (EIS, Zahner IM6ex) were obtained by applying a sine wave with amplitude of 5.0 mV over the frequency range from 100 kHz to 100 mHz. Before EIS tests, the assembled cells were first discharged/charged at a current density of 200 mA g^{-1} for 5 cycles to stabilize the cells. All the tests were performed at 298K.

Results and Discussion

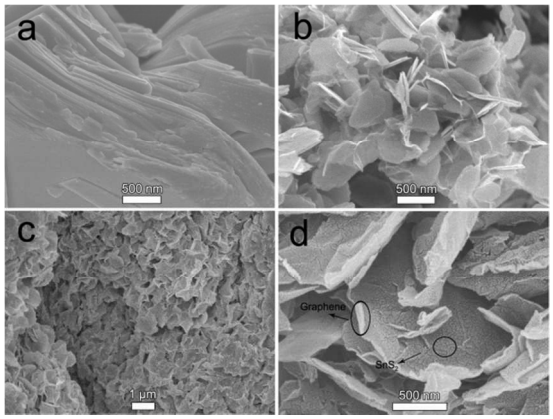

Fig. 1 SEM images of (a) bulk SnS_2, (b) pure restacked SnS_2, (c, d) SnS_2/G-20 nanocomposite.

Fig. 1 presents the SEM images of commercial bulk SnS_2, pure restacked SnS_2, and the SnS_2/G-20 composite. The building blocks of bulk SnS_2 are tightly stacked micrometer-sized nanosheets (Fig. 1a). After hydrolysis of $LiSnS_2$ and subsequent hydrothermal processing, the obtained exfoliated-restacked SnS_2 interestingly changes to highly-scattered nanoflakes (Figure 1b). It should also be noted that the size and thickness of the nanosheets are significantly decreased relative to the bulk phase. When optimum level of graphene oxide (GO) is introduced to the CTAB-functionalized exfoliated SnS_2, the synthesized SnS_2/G-20 nanocomposite displays a three-dimensional (3D) network architecture composed of two-dimensional (2D) nanosheets, as shown in Fig. 1c. Additionally, the high-magnification image (Fig. 1d) demonstrates that SnS_2 nanoplates with ultrasmall size are decorated on the surface of graphene, and distributed uniformly throughout the whole network. On one hand, CTA^+ can act as a connection medium between SnS_2 and GO through electrostatic interaction (with the surface ζ-potential of exfoliated SnS_2 and GO quantified to be -35 mV and -40 mV, respectively); on the other hand, CTA^+-embellished SnS_2 layers do not tend to aggregate, and the incorporated graphene would further suppress their stacking, so the SnS_2 nanoplates restacked on graphene substrate turn out to be extremely small. The 3D architecture of SnS_2/G-20 was attributed to the self-assembly of flexible graphene by partial overlapping or coalescing during the hydrothermal process.[45] By contrast, on adding smaller amounts of GO, although some tiny SnS_2 nanoplates also restack on graphene, the 3D network is not well formed for SnS_2/G-10; whereas excess GO will inevitably block the open-framework structure, and SnS_2/G-30 is overlapped with large areas of graphene (Fig. S1†).

EDS analyses reveal that the SnS_2/graphene composites consist of Sn, S, C, and a small quantity of O and N. The minimal oxygen element comes from the graphene oxide, which is not reduced completely. The existence of N element indicates that N-doped graphene is formed in NH_3 (released from NH_2CSNH_2) atmosphere during the hydrothermal process. It is believed that N-doping can enhance the electric conductivity of graphene and thus improve the electrochemical performance.[47,48] The elemental compositions of the samples with different graphene contents are summarized in Table 1. It is calculated that the atomic ratio of S to Sn ranges from 1.95 to 2.01, approaching the theoretical value of SnS_2. These values confirm that the products are stoichiometric SnS_2. In addition, the EDS mapping of SnS_2/G-20 nanocomposite (Fig. S2†) demonstrates that SnS_2 is homogeneously distributed on graphene substrate throughout the whole network.

Table 1 Elemental compositions of the SnS_2/graphene composites.

Samples	Element (wt.%)				
	Sn	S	C	O	N
SnS_2/G-10	60.18	31.73	5.83	1.69	0.57
SnS_2/G-20	55.30	29.60	11.85	2.23	1.02
SnS_2/G-30	51.03	27.72	16.68	3.01	1.56

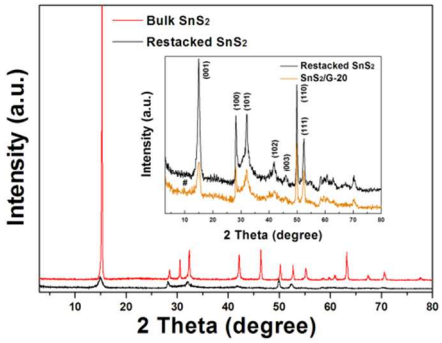

Fig. 2 XRD patterns of bulk SnS_2, pure restacked SnS_2, and SnS_2/G-20 nanocomposite (inset).

XRD patterns of the samples are shown in Fig. 2. As can be seen, bulk SnS_2 exhibits high crystallinity with sharp diffraction peaks, which can be readily indexed to a hexagonal phase (JCPDS No. 23-677). The strong (001) peak with a *d*-spacing of 0.59 nm signifies a well-stacked layered structure along the *c* axis. In comparison, restacked SnS_2 shows broadened peaks and a much shortened (001) peak, indicating that the mean crystallite size and the number of layers along the *c* axis are much smaller than those of raw SnS_2 (from over 70 layers to about 9-10 layers, extracted from the full width at half maximum (FWHM)).[37] Additionally, the positions of the diffraction peaks are slightly shifted toward larger angles relative to pristine SnS_2, corresponding to a small increase in the interplanar spacing.[35] As

for the SnS_2/G-20 nanocomposite, the intensity of the diffraction peaks becomes even weaker compared with restacked SnS_2. This implies that the incorporation of CTAB and graphene further restrains the stacking of SnS_2, and its size comes out to be even smaller, as the SEM images show (Fig. 1). Meanwhile, we can barely detect the (002) diffraction peak of graphene at $2\theta \approx 25°$, indicating that the graphene nanosheets are seldom stacked together. This can be attributed to the SnS_2 nanoplates, which are anchored on the surface of graphene and suppress its stacking. Moreover, a small peak (marked by #) appears at $2\theta = 9.5°$ with a *d*-spacing of ~0.93 nm, which suggests that a very small amount of the graphene is lying in the van der Waals gaps of the host SnS_2, leading to an expansion of the interplanar spacing.[35]

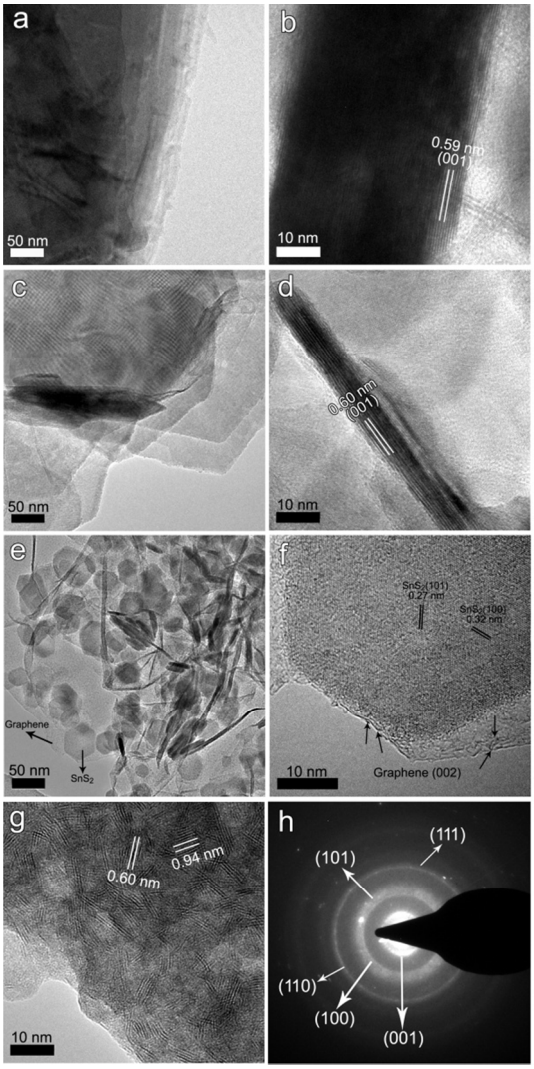

Fig. 3 TEM and HRTEM images of (a, b) bulk SnS_2, (c, d) restacked SnS_2, (e, f, g) SnS_2/G-20 nanocomposite. (h) SAED pattern of SnS_2/G-20.

The microstructures of the samples were subsequently compared by TEM and high-resolution TEM (HRTEM). Fig. 3a and b indicate that bulk SnS_2 has a layered structure composed of tens of layers tightly stacked together. While the size and thickness of the restacked SnS_2 flakes are decreased significantly compared to the bulk, as revealed in Fig. 3c, Fig. 3d further elucidates that the flake is piled up by 9-10 layers, and the interlayer spacing is 0.60 nm, a little larger than that of the raw material (0.59 nm). In SnS_2/G-20 nanocomposite (Fig. 3e and f), ultrasmall SnS_2 nanoplates with sizes in the range of 20-50 nm are anchored on the surface of graphene. From the side view (Fig. 3g), it can be seen the nanoplates consist of 2-5 layers, and disperse homogeneously throughout the whole framework. Interestingly, few of the interlayer distances are enlarged to 0.94 nm with the intercalation of graphene, which is in agreement with the XRD observations. A selected-area electron diffraction (SAED) pattern in Fig. 3h is well-indexed as a pure hexagonal SnS_2 phase, implying that the graphene layers are seldom stacked together.[45]

Further analyses involved FT-IR spectroscopy, XPS, and Raman spectroscopy are displayed in Fig. 4. As shown in Fig. 4a, the FT-IR characteristic peaks of GO appear at around 1737 cm^{-1} (C=O), 1625 cm^{-1} (C=C), 1400 cm^{-1} (C-O), 1350 cm^{-1} (C-OH), 1150 cm^{-1} (C-O), and 1090 cm^{-1} (C-O), respectively, which are in accordance with previous reports.[38,46] For SnS_2/G-20, these vibrations become much weaker and even hard to be detected, implying that the oxygen-containing groups of GO have been largely removed during hydrothermal processing. The degree of GO to graphene conversion can also be verified from the XPS spectra (Fig. 4b). In brief, the C1s XPS peak-fitting results for GO clearly reveal a considerable degree of oxidation with four resolved peaks, corresponding to sp^2-hydridized C-C/C=C and oxygenated functional groups (C-O, C=O and O-C=O). While in the C1s peak-fitting spectrum for SnS_2/G-20, only C-C/C=C, C-O, C=O peaks are present, along with a π-π^* peak, and the relative peak areas of C-O and C=O are much smaller. Together with the disappearance of the O-C=O peak, the results confirm that a reduction process of GO has occurred.[38,49] Additionally, no peaks of elements other than Sn, S, C, O, N are observed in the survey XPS spectrum of SnS_2/G-20 (Fig. S3†), and the atomic ratio of Sn to S is approximately 1:2. The small peak located at 398 eV is originated from N 1s, further suggesting the formation of N-doped graphene. Fig. 4c presents the Raman spectra of bulk SnS_2, SnS_2/G-20, and GO. The dominant peak of pristine SnS_2 at 311 cm^{-1} corresponds to the A_{1g} mode of hexagonal SnS_2.[50] This mode becomes much weaker and broader for SnS_2/G-20, which is particular significant for the decreasing number of SnS_2 layers resulted from the phonon confinement.[36] Moreover, two other Raman peaks at 1350 and 1600 cm^{-1} can be seen in the spectrum of SnS_2/G-20, which are related very well to the D and G bands of graphene. In general, the D band is attributed to defects and disorder in the hexagonal graphitic layers, while the G band is ascribed to the vibration of sp^2 carbon atoms in a 2D hexagonal lattice. Therefore, the intensity ratio of I_D/I_G for SnS_2/G-20 exhibits an enhanced value as compared with that of GO, further proving the formation of graphene with some defects and disordered structure.[38,49]

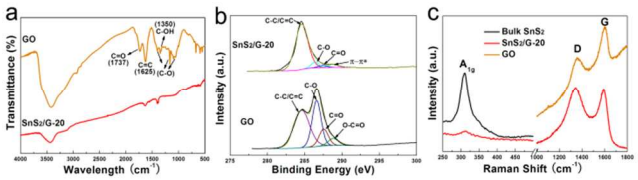

Fig. 4 (a) FT-IR spectra of as-prepared GO and SnS_2/G-20 nanocomposite. (b) C1s XPS spectra of GO and SnS_2/G-20. (c) Raman spectra of bulk SnS_2, SnS_2/G-20, and GO.

The electrochemical reactivity of the SnS_2/G-20 nanocomposite was evaluated by cyclic voltammetry (CV, Fig. 5a). In the first cathodic scan, two peaks at higher voltage (1.85 and 1.55 V) are commonly assigned to sodium intercalation into the SnS_2 layers without phase decomposition:[43]

$$x\mathrm{Na}^+ + \mathrm{SnS}_2 + xe^- \rightarrow \mathrm{Na}_x\mathrm{SnS}_2 \quad (1)$$

The broad cathodic peak ranging from 0.3-0.7 V could be attributed to the conversion and alloying reactions (eqn (2) and (3)), as well as the formation of irreversible solid electrolyte interphase (SEI) in the 1st cycle. This peak shifts to 0.58 V in subsequent scans, which is consistent with previous reports.[33,43,44]

$$4\mathrm{Na}^+ + \mathrm{SnS}_2 + 4e^- \rightarrow 2\mathrm{Na}_2\mathrm{S} + \mathrm{Sn} \quad (2)$$

$$\mathrm{Sn} + 3.75\mathrm{Na}^+ + 3.75e^- \rightarrow \mathrm{Na}_{3.75}\mathrm{Sn} \quad (3)$$

In the anodic scan, the broad oxidation peak at 1.3 V corresponds to the desodiation reaction of Na_xSn. The well overlapping of this peak in all cycles indicates the high reversibility of the reaction in eqn (3). The distinct anodic peak at 2.1 V could be attributed to the oxidation of Sn to SnS_2 and the sodium extraction from Na_xSnS_2. It should be noted that this peak becomes weaker and weaker from the 1st to the 7th cycle, implying the reaction in eqn (2) is partially reversible (similar to the reconstitution of SnS_2 in lithium ion batteries).[30,49,51] And it is why the cathodic peaks corresponding to the formation of Na_xSnS_2 become much weaker from the 2nd cycle. Moreover, the small reduction peak at 0.01 V and the oxidation peak at 1.65 V are assigned to Na^+ storage/release on graphene.[52]

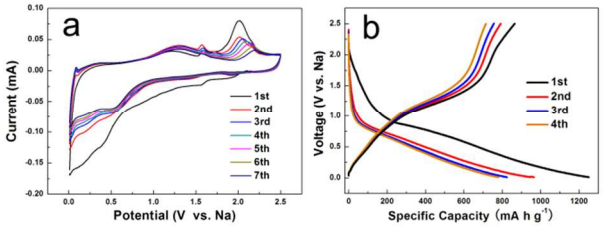

Fig. 5 (a) Cyclic voltammetry curves of SnS_2/G-20 electrode scanned between 0.01-2.5 V at a rate of 0.1 mV s^{-1}. (b) Initial four galvanostatic charge-discharge profiles of SnS_2/G-20 electrode at a current density of 200 mA g^{-1}.

Fig. 5b shows the first four galvanostatic charge-discharge profiles of SnS_2/G-20 nanocomposite at a current density of 200 mA g^{-1}. In consistent with the above CV study, a small plateau at 1.6-1.8 V is observed in the first discharge process, which is attributed to the formation of Na_xSnS_2. Another plateau at 0.4-0.8 V corresponds to the conversion and alloying reaction process, in the meantime, a gel-like polymeric layer is formed resulting from electrochemically driven electrolyte degradation. This conspicuous plateau can also be observed in the following discharge curves. In the charge profiles, SnS_2/G-20 exhibits a superimposed plateau at ~1.0 V and a fading plateau at 2.1 V, which also agree with the previous CV curves. In addition, during the first cycle, the sodiation and desodiation capacities are 1250.1 mA h g^{-1} and 864.5 mA h g^{-1}, respectively, corresponding to a high coulombic efficiency (CE) of 69%. The capacity decrease in the initial cycles is caused by the formation of an irreversible SEI film on the electrode and the partially reversible reconstitution of SnS_2.

Fig. 6a depicts the cycling performance of the as-synthesized samples evaluated at a discharge current density of 200 mA g^{-1}. Bulk SnS_2 electrode delivers a diminishing discharge capacity from over 300 mA h g^{-1} during the initial cycles to 54.3 mA h g^{-1} in the 100th cycle (with capacity retention of only 16.5 %). After exfoliation, the restacked SnS_2 shows a higher capacity of more than 400 mA h g^{-1}, but the cyclability is still poor, with only 60.9 mA h g^{-1} retained after 100 cycles (capacity retention of 14.5 %). When incorporating graphene on this basis, the discharge capacity and cyclic stability of the SnS_2/graphene compomsites are greatly enhanced. Particularly, SnS_2/G-20 electrode displays a remarkable capacity, as high as 650 mA h g^{-1} when the capacity is stable, and the capacity still maintains 618.9 mA h g^{-1} in the 100th cycle (capacity retention of 95.2 %). Insufficient graphene addition is not favorable for the formation of the 3D network architecture with ultrasmall SnS_2 nanoplates, whereas too much graphene will significantly block the channels for Na^+ ion diffusion. Consequently, the electrochemical performances of SnS_2/G-10 and SnS_2/G-30 are not comparable with that of SnS_2/G-20. Fig. 6b further demonstrates that the SnS_2/G-20 electrode exhibits good rate capability with a high CE (~99%). When the current density is increased in steps to 500, 1000, 2000, and 4000 mA g^{-1}, the corresponding reversible capacity can reach 532, 461, 381, and 326 mA h g^{-1}, respectively, which is still higher than that of bulk SnS_2 or pure graphene (Fig. S4†). More importantly, when the current density is returned to 200 mA g^{-1}, the capacity swiftly recovers to ~610 mA h g^{-1} within a few cycles and remains stable without fading up to 300 cycles. The achieved electrochemical performance of SnS_2/G-20 also compares favorably with that of previously reported SnS_2 anode for SIBs.[33,34,43,44]

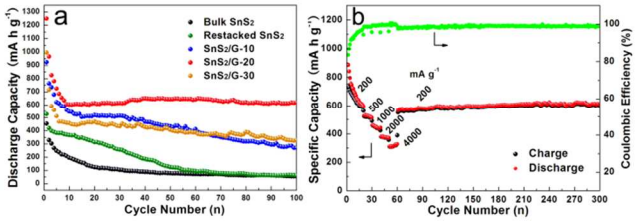

Fig. 6 (a) Cycling behavior of the synthesized samples: bulk SnS_2, restacked SnS_2, SnS_2/G-10, SnS_2/G-20, and SnS_2/G-30 at 200 mA g^{-1}. (b) Rate capability and coulombic efficiency of SnS_2/G-20 electrode.

Furthermore, the morphological and structural changes in representative electrodes after charge/discharge cycling were examined using SEM and TEM. Fig. 7a and b confirm that the 3D network architecture of SnS_2/G-20 is retained after 100 cycles at 200 mA g^{-1}. Although the SnS_2 would decompose during cycling, the graphene substrate could effectively inhibit the aggregation of the generated Sn grains and amorphous Na_2S. The active material with ultrasmall size is still homogeneously distributed on the surface of graphene (Fig. 7c) and can continuously maintain the accessibility to the electrolyte, thus also maintaining the high utilization rate for Na-storage with high capacity. On the contrary, as displayed in Fig. 7d, e, and f, the original lamellar restacked SnS_2 changes to big solid bulks agglomerated from a great many pulverized particles after 100

cycles. Such a structure is bound to hinder the infiltration of electrolyte and the diffusion kinetics of Na^+. So, it is not difficult to understand the poor cycling stability of restacked SnS_2.

The electrochemical impedance spectra (EIS) of bulk SnS_2, restacked SnS_2 and SnS_2/G-20 electrodes are compared in Fig. 8. The resistance of the restacked SnS_2 is much lower than that of bulk SnS_2, implying that smaller SnS_2 plates with fewer stacked layers can facilitate the transportation of Na^+ ions. Moreover, the even lower impedance of SnS_2/G-20 demonstrates that the incorporation of graphene effectively enhances the conductivity of SnS_2. In general, the excellent electrochemical performance of SnS_2/G-20 as Na-storage anode can be ascribed to the synergetic effects between the ultrasmall SnS_2 and the highly conductive graphene. These can be interpreted as follows: first, the tiny SnS_2 nanoplates (20-50 nm in size) composed of 2-5 layers, as well as the few enlarged interlayer spacing, are readily accessible to the electrolyte, which can facilitate the reversible Na^+ diffusion kinetics, thus ensuring the full utilization of active materials with high capacity. Second, the introduction of N-doped graphene matrix not only offers a three-dimensional conductive network and effective buffering for volume fluctuation, but also avoids the aggregation of active materials during sodiation/desodiation process. This is beneficial for high-rate capability and long-cycle life.

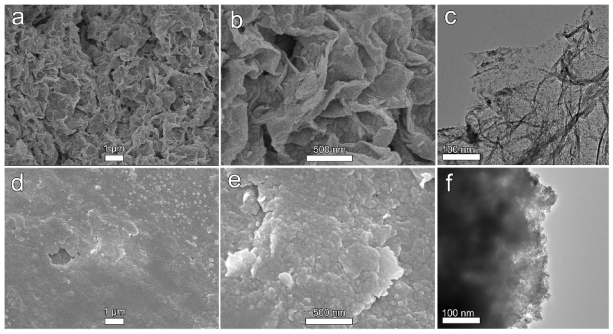

Fig. 7 SEM and TEM images of (a, b, c) SnS_2/G-20 electrode and (d, e, f) restacked SnS_2 electrode after 100 charge/discharge cycles at 200 mA g^{-1}.

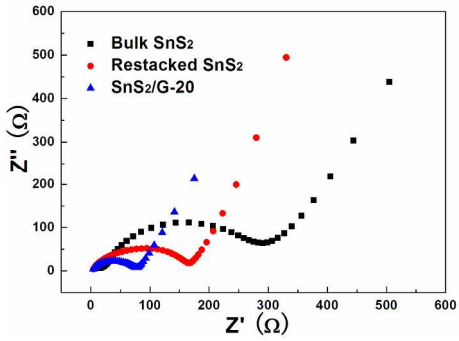

Fig. 8 Electrochemical impedance spectra of bulk SnS_2, restacked SnS_2, and SnS_2/G-20 electrodes.

Conclusion

In summary, exfoliated-SnS_2 restacked on graphene has been prepared by the hydrolysis of lithiated SnS_2 followed by a facile hydrothermal method. The as-prepared SnS_2/graphene nanocomposite displays a 3D network architecture with the ultrasmall SnS_2 nanoplates (composed of 2-5 layers, with typical size of 20-50 nm) decorated homogeneously on the surface of graphene. When used as anode material for sodium ion batteries, the unique structure can effectively facilitate the reversible Na^+ diffusion kinetics and ensure the full utilization of active materials upon prolonged cycling. Consequently, the obtained SnS_2/graphene nanocomposite exhibits much higher specific capacity as well as superior cyclic stability compared to bulk SnS_2. It can deliver a remarkable capacity as high as 650 mA h g^{-1} at the current density of 200 mA g^{-1}. More impressively, the capacity can reach 326 mA h g^{-1} even at 4000 mA g^{-1} and remains stable at ~610 mA h g^{-1} without fading up to 300 cycles when the rate is brought back to 200 mA g^{-1}. This result should shed light on the potential application of SnS_2 or other layered metal sulfides (*e.g.*, MoS_2, TiS_2, and WS_2) as high-performance electrode for sodium-ion batteries.

Acknowledgements

The authors gratefully acknowledge the financial support for this research from the 973 program (2010CB631303), NSFC (51171083), MOE Innovation Team (IRT-13R30 and IRT13022) and 111 Project (B12015).

Notes and references

Key Laboratory of Advanced Energy Materials Chemistry (MOE), College of Chemistry, Collaborative Innovation Center of Chemical Science and Engineering, Nankai University, Tianjin 300071, P.R. China, Tel.: +86 22 23504527; fax: +86 22 23504527; E-mail: jiaolf@nankai.edu.cn

†Electronic Supplementary Information (ESI) available: [Scheme S1, Fig. S1-S4]. See DOI: 10.1039/b000000x/

1 B. Dunn, H. Kamath and J. M. Tarascon, *Science*, 2011, **334**, 928.
2 L. Fu, K. Tang, K. Song, P. A. van Aken, Y. Yu and J. Maier, *Nanoscale*, 2014, **6**, 1384.
3 J. B. Goodenough, *Acc. Chem. Res.*, 2013, **46**, 1053.
4 V. Palomares, P. Serras, I. Villaluenga, K. B. Hueso, J. Carretero-Gonzalez and T. Rojo, *Energy Environ. Sci.*, 2012, **5**, 5884.
5 B. L. Ellis and L. F. Nazar, *Curr. Opin. Solid State Mater. Sci.*, 2012, **16**, 168.
6 M. D. Slater, D. Kim, E. Lee and C. S. Johnson, *Adv. Funct. Mater.*, 2013, **23**, 947.
7 S. W. Kim, D. H. Seo, X. H. Ma, G. Ceder and K. Kang, *Adv. Energy Mater.*, 2012, **2**, 710.
8 H. L. Pan, Y. S. Hu and L. Q. Chen, *Energy Environ. Sci.*, 2013, **6**, 2338.
9 C. D. Wessells, S. V. Peddada, R. A. Huggins and Y. Cui, *Nano Lett.*, 2011, **11**, 5421.
10 N. Yabuuchi, M. Kajiyama, J. Iwatate, H. Nishikawa, S. Hitomi, R. Okuyama, R. Usui, Y. Yamada and S. Komaba, *Nat. Mater.*, 2012, **11**, 512.
11 S. Xin, Y. X. Yin, Y. G. Guo and L. J. Wan, *Adv. Mater.*, 2014, **26**, 1261.
12 Y. Zhu, Y. Xu, Y. Liu, C. Luo and C. S. Wang, *Nanoscale*, 2013, **5**, 780.
13 C. Zhu, X. Mu, P. A. van Aken, Y. Yu and J. Maier, *Angew. Chem. Int. Ed.*, 2014, **53**, 2152.
14 Y. U. Park, D. H. Seo, H. S. Kwon, B. Kim, J. Kim, H. Kim, I. Kim, H. L. Yoo and K. Kang, *J. Am. Chem. Soc.*, 2013, **135**, 13870.
15 K. Sakaushi, E. Hosona, G. Nickerl, T. Gemming, H. Zhou, S. Kaskel and J. Eckert, *Nat. Commun.*, 2013, **4**, 1485.
16 J. Liu, K. Tang, K. Song, P. A. van Aken, Y. Yu and J. Maier, *Nanoscale*, 2014, **6**, 5081.
17 V. L. Chevrier and G. Ceder, *J. Electrochem. Soc.*, 2011, **158**, A1011.
18 G. Pang, C. Z. Yuan, P. Nie, B. Ding, J. Zhu and X. G. Zhang, *Nanoscale*, 2014, **6**, 6328.

19 W. Li, S. L. Chou, J. Z. Wang, J. H. Kim, H. K. Liu and S. X. Dou, *Adv. Mater.*, 2014, **26**, 4037.
20 L. Wu, X. H. Hu, J. F. Qian, F. Pei, F. Y. Wu, R. J. Mao, X. P. Ai, H. X. Yang and Y. L. Cao, *Energy Environ. Sci.*, 2014, **7**, 323.
21 L. D. Ellis, T. D. Hatchard and M. N. Obrovac, *J. Electrochem. Soc.*, 2012, **159**, A1801.
22 H. L. Zhu, Z. Jia, Y. C. Chen, N. Weadock, J. Y. Wan, O. Vaaland, X. G. Han, T. Li and L. B. Hu, *Nano Lett.*, 2013, **13**, 3093.
23 Y. H. Xu, Y. J. Zhu, Y. H. Liu and C. S. Wang, *Adv. Energy Mater.*, 2013, **3**, 128.
24 L. W. Ji, M. Gu, Y. Y. Shao, X. L. Li, M. H. Engelhard, B. W. Arey, W. Wang, Z. M. Nie, J. Xiao, C. M. Wang, J. G. Zhang and J. Liu, *Adv. Mater.*, 2014, **26**, 2901.
25 B. Farbod, K. Cui, W. P. Kalisvaart, M. Kupsta, B. Zahiri, A. Kohandehghan, E. M. Lotfabd, Z. Li, E. J. Luber and D. Mitlin, *ACS Nano*, 2014, **8**, 4415.
26 Y. H. Liu, Y. H. Xu, Y. J. Zhu, J. N. Culver, C. A. Lundgren, K. Xu and C. S. Wang, *ACS Nano*, 2013, **7**, 3627.
27 D. W. Su, C. Y. Wang, H. J. Ahn and G. X. Wang, *Phys. Chem. Chem. Phys.*, 2013, **15**, 12543.
28 D. W. Su, H. J. Ahn and G. X. Wang, *Chem. Commun.*, 2013, **49**, 3131.
29 L. Wu, X. H. Hu, J. F. Qian, F. Pei, F. Y. Wu, R. J. Mao, X. P. Ai, H. X. Yang and Y. L. Cao, *J. Mater. Chem. A*, 2013, **1**, 7181.
30 J. Seo, J. Jang, S. Park, C. Kim, B. Park and J. Cheon, *Adv. Mater.*, 2008, **20**, 4269.
31 Y. Du, Z. Yin, X. Rui, Z. Zeng, X. J. Wu, J. Liu, Y. Zhu, J. Zhu, X. Huang, Q. Yan and H. Zhang, *Nanoscale*, 2013, **5**, 1456.
32 J. Qian, Y. Xiong, Y. Cao, X. Ai and H. X. Yang, *Nano Lett.*, 2014, **14**, 1865.
33 B. H. Qu, C. Z. Ma, G. Ji, C. H. Xu, J. Xu, Y. S. Meng, T. H. Wang and J. Y. Lee, *Adv. Mater.*, 2014, **26**, 3854.
34 T. Zhou, W. K. Pang, C. Zhang, J. Yang, Z. Chen, H. K. Liu and Z. P. Guo, *ACS Nano*, 2014, **8**, 8323.
35 E. Aharon, A. Albo, M. Kalina, G. L. Frey, *Adv. Funct. Mater.*, 2006, **16**, 980.
36 Z. Y. Zeng, Z. Y. Yin, X. Huang, H. Li, Q. Y. He, G. Lu, F. Boey and H. Zhang, *Angew. Chem. Int. Ed.*, 2011, **50**, 11093.
37 G. D. Du, Z. P. Guo, S. Q, Wang, R. Zeng, Z. X. Chen and H. K. Liu, *Chem. Commun.*, 2010, **46**, 1106.
38 Y. C. Liu, Y. P. Zhao, L. F. Jiao and J. Chen, *J. Mater. Chem. A*, 2014, **2**, 13109.
39 S. Lu, Y. Cheng, X. Wu and J. Liu, *Nano Lett.*, 2013, **13**, 2485.
40 Y. Cheng, H. Zhang, S. Lu, C. V. Varanasi and J. Liu, *Nanoscale*, 2013, **5**, 1067.
41 C. X. Guo, X. T. Zheng, Z. S. Lu, X. W. Lou and C. M. Li, *Adv. Mater.*, 2010, **22**, 5164.
42 J. Z. Wang, C. Zhong, D. Wexler, N. H. Idris, Z. X. Wang, L. Q. Chen and H. K. Liu, *Chem. -Eur. J.*, 2011, **17**, 661.
43 X. Q. Xie, D. W. Su, S. Q. Chen, J. Q. Zhang, S. X. Dou and G. X. Wang, *Chem. Asian J.*, 2014, **9**, 1611.
44 P. V. Prikhodchenko, D. Y. W. Yu, S. K. Batabyal, V. Uvarov, J. Gun, S. Sladkevich, A. A. Mikhaylow, A. G. Medvedev and O. Lev, *J. Mater. Chem. A*, 2014, **2**, 8431.
45 K. Chang and W. X. Chen, *ACS Nano*, 2011, **5**, 4720.
46 Y. C. Liu, L. F. Jiao, Q. Wu, Y. P. Zhao, K. Z. Cao, H. Q. Liu, Y. J. Wang and H. T. Yuan, *Nanoscale*, 2013, **5**, 9562.
47 A. L. M. Reddy, A. Srivastava, S. R. Gowda, H. Gullapalli, M. Dubey and P. M. Ajayan, *ACS Nano*, 2010, **4**, 6337.
48 X. Wang, X. Cao, L. Bourgeois, H. Guan, S. Chen, Y. Zhong, D. M. Tang, H. Li, T. Zhai, L. Li, Y. Bando and D. Golberg, *Adv. Funct. Mater.*, 2012, **22**, 2682.
49 S. Liu, X. Lu, J. Xie, G. Cao, T. Zhu and X. Zhao, *ACS Appl. Mater. Interfaces*, 2013, **5**, 1588.
50 B. Luo, Y. Fang, B. Wang, J. S. Zhou, H. H. Song and L. J. Zhi, *Energy Environ. Sci.*, 2012, **5**, 5226.
51 X. W. Lou, C. M. Li and L. A. Archer, *Adv. Mater.*, 2009, **21**, 2536.
52 Y. X. Wang, S. L. Chou, H. K. Liu and S. X. Dou, *Carbon*, 2013, **57**, 202.